



Interfacial engineering strategy based on polymer modification to regulate the residual stress in CsPbI₂Br based perovskite solar cells

Kanghui Zheng ^{a,b}, Chang Liu ^{b,*}, Kuibao Yu ^a, Yuanyuan Meng ^a, Xu Yin ^a, Shixiao Bu ^b, Bin Han ^b, Cuirong Liu ^{a,*}, Ziyi Ge ^{b,*}

^a College of Materials Technology and Engineering, Taiyuan University of Science and Technology, Taiyuan 030024, PR China

^b Ningbo Institute of Materials Technology and Engineering, Chinese Academy of Sciences, Ningbo 315201, PR China



ARTICLE INFO

Keywords:

CsPbI₂Br
J71
Grain size
Phase stability
Interface modification
Microstrains

ABSTRACT

All-inorganic perovskite solar cells have been developed rapidly in the field of photovoltaics due to their excellent photothermal stability. Whereas, the phase stability issues of the inorganic perovskite, caused by the significant residual stress in the film, severely limits the practical applications of inorganic perovskite solar cells (PSCs). Herein, we propose the utilization of organic polymer J71 with N- and S-atoms to release the internal stress in the CsPbI₂Br film. It is uncovered that the coordination between J71 and perovskite could effectively regulate the strain from tensile- to compressive-type, among which the strain-free film could be realized at an optimal J71 concentration. Moreover, we revealed that the covalent bond between J71 and perovskite could induce the secondary crystal growth of CsPbI₂Br during thermal annealing, which leads to refined film morphology in terms of larger and compact perovskite grains. Additionally, J71 molecule with strong hydrophobicity serves as a barrier to block the moisture evasion, which prevents the lattice distortion of [PbI₆]⁴⁻ triggered by water molecules. Owing to the synergistic effects of J71 treatment, the CsPbI₂Br based PSCs achieved an excellent PCE of 16.15%, with outstanding stability by retaining over 80% of the initial PCEs under both N₂ and humid environment.

1. Introduction

All-inorganic perovskites CsPbX₃ have attracted tremendous attentions because of their excellent heat resistance and well-preserved crystal structure under light illuminations [1]. Among the CsPbX₃ family, CsPbI₂Br has stood out due to its balance between the optical bandgap and phase stability. However, CsPbI₂Br is ultrasensitive to humidity, which drives the transition of CsPbI₂Br from photoactive black phase (α phase) to non-photoactive yellow phase (δ phase) even under low relative humidity (RH) environment [2]. Hu et al. found that there is a close relationship between the internal stress of CsPbI₂Br and its phase transition. Herein, an $\alpha \rightarrow \delta \rightarrow \alpha$ phase transition growth (PTG) approach is developed for the deposition of CsPbI₂Br films that allows relaxation of the relative tensile strain by $62 \pm 4\%$ and increases the domain size by 800%. The relaxation of internal force can greatly improve the efficiency and stability of the device [3]. Many research indicate that the existence of tensile stress in all inorganic perovskite is responsible for the phase instability under room temperature in

ambient, and suggest that dispersion of the internal stress would be an effective means to maintain the black phase [4]. In addition, the tensile stress in the film leads to the lattice expansion of CsPbI₂Br, which is prone to high defect density and serious non-radiative recombination loss of the devices [5]. It thus limits the photovoltaic performance of CsPbI₂Br based PSCs.

Towards the end of releasing the internal stresses generated during film deposition process, two-step annealing treatment has been widely brought up, in which the first step annealing is performed at lower temperatures of 40–60 °C [6–8]. It has been demonstrated to be an effective means to relax the lattice stress during the first annealing step and ensure the preferred growth of the crystal plane (1 0 0) of CsPbI₂Br perovskite film. The PSCs with two-step annealing treatment achieved power conversion efficiency (PCE) over 15%, with 200-hours phase stability under RH25%[9]. Whereas, it is noted that the CsPbI₂Br is extremely sensitive to the growth temperature of the first annealing step, which needs to be strictly controlled. Otherwise, it would easily result in the non-uniformity of crystal growth and the production of

* Corresponding authors.

E-mail addresses: liuchang1@nimte.ac.cn (C. Liu), lcr@tyust.edu.cn (C. Liu), geziyi@nimte.ac.cn (Z. Ge).

mesophases [10]. It thus complicates the fabrication procedure and makes it difficult to be adapted in scalable deposition process. Other approaches such as metal cation alloying has also been reported [8,11–14]. Metal cations including Rb^+ , In^{3+} , Sn^{2+} , Fe^{2+} , and Cu^{2+} were doped into perovskite to regulate the thermal expansion coefficient and heat resistance of the film, which could release the lattice stress generated during the thermal annealing process [15–17]. However, it would also alter the electronic band structure of the system, which may be adverse to the photovoltaic efficiency. Additionally, humidity is a serious issue that would aggravate the phase degradation, which is yet lack of concern. Therefore, it is urgent to find a dual protection strategy to tackle the stability issues aroused by the tensile stress of the crystal lattice and the moisture invasion into the film [18].

Herein, we applied the organic molecule J71 [19] (the molecular structure is shown in Fig. 1b) with Lewis base properties to regulate the perovskite crystallization. The S-rich and N-rich elements in the molecule can coordinate with the under coordinated Pb^{2+} to form Lewis complex, which could effectively suppress the lattice distortion of $[\text{PbI}_6]^{4-}$ octahedron and reduce the defect state. Moreover, the strong coordination interaction between J71 and perovskite could induce the secondary growth of perovskite films as well, which led to the refined crystal morphology with larger grain size and homogeneously distributed crystals. By this, we revealed that the lattice distortion could be circumvented, and the stress within perovskite lattices are released. As a result, the PSCs with J71 treatment delivers an outstanding PCE of 16.15% with an impressive V_{OC} of 1.28 V. In addition, J71 molecule with strong hydrophobicity serves as a barrier to block the moisture evasion, which drastically improves the stability of inorganic PSCs. The device retains over 80% of its initial PCE after aging in humidity environment for 650 h, respectively, which is one of the highest moisture stability for inorganic PSCs to date.

2. Experimental

2.1. Materials and reagents

SnO_2 -colloid precursor (tin (IV) oxide, 15% in H_2O colloidal dispersion), N,N-dimethyl formamide (DMF, 99.8%), Dimethyl sulfide (DMSO, 99.7%), and chlorobenzene (CB, 99.9%) were purchased from Beijin J&K Scientific Ltd. Cesium iodide (CsI , 99.99%), lead(II) iodide (PbI_2 , 99.99%), lead(II) bromide (PbBr_2 , 99.99%), 2,2',7,7'-tetraakis[N,N-di(4-methoxyphenyl)amine]-9,9'-spirobifluorene (spiro-OMeTAD, 99.8%) lithium bis (trifluoromethanesulfonyl) imide (Li-TFSI , 99%), 4-tertbutylpyridine (TBP, 96%) and tris (2-(1H-pyrazol-1-yl)-4-tert-butylpyridine)-cobalt(III) tris [bis (trifluoromethylsulfonyl) imide] (FK209, 99.5%) were purchased from Xi'an Polymer Light Technology Corporation. J71 was purchased from Shuolun organic photoelectric technology Corporation. All these commercially available materials were used directly as received without any further purification.

2.2. Precursor preparation and devices fabrication

PbI_2 (276.6 mg), PbBr_2 (220.2 mg), CsI (312 mg) (molar ratio 0.6:0.6:1.2) were mixed and dissolved in 1 ml of solvent (DMF:DMSO = 7:3) to prepare the precursor of perovskite solution. The solution is stirred and heated in N_2 environment at 80 °C and left overnight to achieve full dissolution of the solution. Filter the perovskite precursor with a 0.22 μl filter before use.

J71 were dissolved in chlorobenzene with different concentrations and stirred for 2 h for complete dissolution (concentrations of 0.5 mg/mL, 0.8 mg/mL, 1 mg/mL and 2 mg/mL, respectively).

The etched ITO was washed with detergent, deionized water, acetone, and isopropanol in sequence for 30 min. The cleaned ITO/glass substrate was dried by N_2 gas and then treated with ultraviolet ozone for 45 min. Dilute the existing 15% concentration of SnO_2 colloidal water with deionized water (SnO_2 : H_2O = 2:1). The diluted SnO_2 precursor

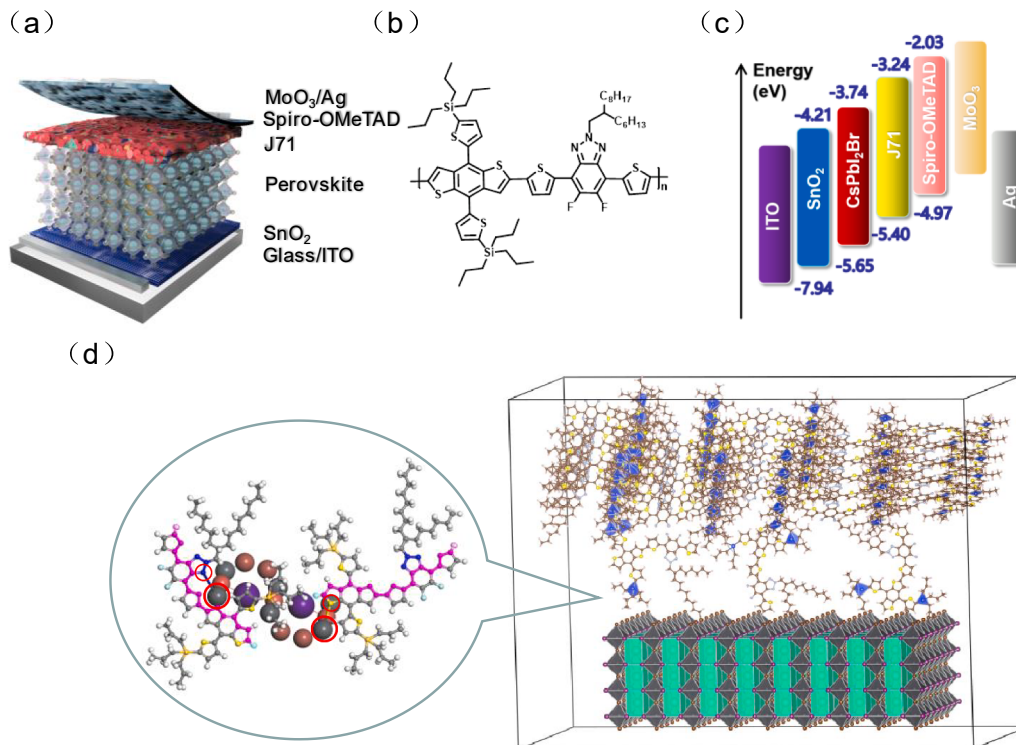


Fig. 1. (a) Illustration of as-prepared CsPbI_2Br solar cells with the structure of ITO/ SnO_2 /Perovskite/J71/Spiro-OMeTAD/ MoO_3 /Ag, (b) molecular formula of J71, (c) Energy level diagrams of PSCs, (d) Schematic diagram of interaction between CsPbI_2Br and J71.

solution was spin-coated on ITO glass for 10 s at 6500 rpm, and then annealed at 150 °C for 30 min. In a N₂ atmosphere, the prepared CsPbI₂Br precursor solution was deposited on the SnO₂ substrate by a two-step spin coating process: 1000 rpm for 6 s followed by 3000 rpm for 30 s. The as-casted film was then annealed at 50 °C for 80 s and then at 180 °C for 5 min to form the required α-phase CsPbI₂Br. Take out the annealed hot perovskite substrate quickly, and quickly spin coat the 150 °C heated J71 chlorobenzene solutions of different concentrations on the hot perovskite at 5000 rpm, and cool naturally after spin coating. Then the Spiro-OMeTAD film was spin-coated on the film at 4000 rpm for 30 s. The Spiro-OMeTAD solution contained 72.5 mg Spiro-OMeTAD, 18 μL of LiTFSI stock solution (520 mg/mL in acetonitrile) and 29 μL of FK209 solution (300 mg/mL in acetonitrile) and 29 μL of tBP. Finally, 8 nm MoO₃ and 100 nm Ag electrodes were thermally evaporated to complete the fabrication of the entire device. The effective area of all devices is 0.04 cm².

2.3. Characterizations

The photovoltaic performance of the device was measured under the simulated solar lamp (100 mW cm⁻² AM 1.5G) provided by Newport oriel sol3a 450 W solar simulator. The J-V curves of PSCs were measured at room temperature. The light source parameters are 450 W xenon lamp (oriel solar simulator), calibrated to 100 MW cm⁻² by silicon reference cell. The scanning parameters were forward scanning (2 to -0.5 V, step 0.02 V) and reverse scanning (from -0.5 to 2 V, step 0.02 V). Choose the scan rate between 0.01 and 0.5 V s⁻¹. The EQE spectra were recorded by using the solar cell quantum efficiency test system (Elli Technology Taiwan). TEM images were taken by Talos f200× (Themo Fisher, USA). To imitate the film morphology in actual devices, perovskite and perovskite/J71 films were prepared on ITO substrates, which were then scraped off from the substrates, followed by dispersing the powders in toluene solvent. Subsequently dropping the dispersion onto the copper grid (400 mesh) for TEM measurement. X-ray photoelectron spectroscopy (XPS) and he-I (21.22ev) emission lines were measured by Kratos axial super dald. SEM images were obtained by scanning electron microscope (verios G4 UC) (rimono scientific company, USA) at 5 kV. The steady PL spectra were recorded on the Horiba jobin Yvon fluorolog-3 spectrophotometer system. The incident light at 510 nm on the ITO surface leads to photon excitation. Time resolved fluorescence was measured and analyzed by Edinburgh instrument. TRPL decay excitation was also detected by FLS 980 fluorescence spectrometer. Convolution fitting analysis was used at 625 nm to measure samples. Attenuation is a term applied to the function of three exponential models. The quality of fitting depends on the parameters χ² estimate ($0.90 \leq \chi^2 \leq 1.10$). Chi 660e electrochemical measurement workstation (Chengdu equipment company, Shanghai, China) was used for SCLC analysis under dark conditions. And the C²-V spectra were conducted on Chenhua CHI760E electrochemical workstation. The electrochemical analyzer (AMETEK, Inc., berwen, USA) uses different bias voltages in the frequency range of 0.1 to 10⁵ Hz. Raman spectra were collected using a Confocal Raman Spectrometer (RENISHAW). A laser excitation wavelength of 633 nm was utilized. A threshold power of ~ 0.5 mW was kept throughout the measurements to avoid the potential laser-induced heating on the samples. Before the measurements, the Raman system was calibrated using the Raman mode of a silicon wafer at 520 cm⁻¹. Depth resolved GIXRD were characterized using a Rigaku SmartLab five-axis X-ray diffractometer at 45 kV and 200 mA, equipped with Cu Kα radiation ($\lambda = 1.54050 \text{ \AA}$), parallel beam optics and a secondary graphite monochromator. Before the test, the X-ray diffraction on well recrystallized LaB₆ powders was used for subtle alignment of instrument, the acceptable LaB₆ peak shift is less than 0.01° in 2θ comparing to its JCPDF file. For the residual stress tests, a slow scan rate of 0.12° min⁻¹ was carried out to ensure fine structural information.

3. Results and discussion

In this work, the p-type polymer (J71) is selected to relax the lattice strain of all-inorganic perovskite. The structure of n-i-p device and molecular formula of J71 are illustrated in Fig. 1a, b respectively. According to the previous report, J71 has a highest occupied molecular orbital (HOMO) level of -5.40 eV,[19] which is well-aligned with those of the perovskite (-5.65 eV) and Spiro-OMeTAD (-4.97 eV) for efficient hole extraction, as illustrated in Fig. 1c. Fig. 1d illustrates the schematic diagram of the interactions between J71 and perovskite, where the S and N atoms with lone pair electrons in J71 form Lewis complexes with unpaired Pb atoms in perovskite [19]. Because some Lewis bases can coordinate with perovskite Pb (II) halides through chelation, the morphology and grain size of perovskite materials can be effectively controlled. On the other hand, some passivators containing N-donor and O-donor form Lewis acid-base adducts with under coordination Pb²⁺ defects in perovskite. This adduct can effectively reduce the activation energy and realize the secondary growth of perovskite grains [20]. The coordination would on one side passivate the defect states in the perovskite film, and on the other side trigger the heterogeneous nucleation of CsPbI₂Br for secondary crystallization during thermal annealing, which could release the residual stress in the CsPbI₂Br film [21].

In order to characterize the bonding between J71 and CsPbI₂Br, X-ray photoelectron spectroscopy (XPS) measurement has been conducted to trace the elements and analyze the binding energy of the film surface. Fig. 2a shows the full spectra of J71, CsPbI₂Br and CsPbI₂Br/J71 films. Compared to the pristine CsPbI₂Br film, the CsPbI₂Br/J71 film shows the signals from F, N, S, Si elements, confirming the existence of J71 on the film surface. The high-resolution XPS spectra of Pb 4f, N 1s and S 2s are then studied, the results are presented in Fig. 2b-d. The Pb 4f core-level spectrum of the CsPbI₂Br film shows two strong peaks at 142.90 and 138.03 eV (corresponding to 4f 5/2 and 4f 7/2, respectively), which shift by 0.28 and 0.28 eV toward lower binding energy for CsPbI₂Br/J71 film. On the contrary, the N 1s and S 2s signals of CsPbI₂Br/J71 film shift by 0.55 eV and 0.14 eV toward higher binding energy, respectively, as compared with those of the CsPbI₂Br film [22]. According to the principle of chemical shift caused by the state of the element change, it can be proved that the lone pair electrons from N and S atoms are coordinated with Pb atoms upon the formation of Pb-N and Pb-S covalent bond, which could fill the grain boundaries and release the tensile strain at the grain boundary [22,23].

The steady-state photoluminescence (PL) and time-resolved photoluminescence (TRPL) measurements have then been carried out to study the carrier recombination dynamics in the perovskite films, as shown as Fig. 3a-b. From Fig. 3a, it is observed that the CsPbI₂Br film with J71 exhibits an obvious PL quenching as compared to the control film, which should be ascribed to the p-type characteristic of J71 for hole transporting [24]. Meanwhile, the PL peak experienced a blue-shift from 651.8 nm to 644.5 nm with J71 treatment, suggesting the reduced trap-assisted recombination in CsPbI₂Br film with J71 passivation [25,26]. The TRPL spectra (Fig. 3b) have then been double exponential function fitted according to the equation: $F(t) = A_1 \exp(-t/\tau_1) + A_2 \exp(-t/\tau_2)$, where short-lifetime τ_1 corresponds to the surface recombination, the long-lifetime τ_2 presents the bulk recombination, and A_1 and A_2 are the related amplitudes. The average lifetime is determined by $\langle \tau \rangle = \alpha_1 \tau_1 + \alpha_2 \tau_2$, $\alpha_i = A_i \tau_i / \sum A_i \tau_i$ [27], and the fitting parameters are summarized in Table S1. It is observed that CsPbI₂Br/J71 shows longer τ of 15.897 ns than that of pristine film of 1.044 ns, indicative of suppressed traps with J71 treatment. The PL and TRPL results substantiate the role of J71 to accelerate hole transport and defect passivation at the mean time [28,29].

The effects of J71 on the morphological features of CsPbI₂Br film are further examined by scanning electron microscope (SEM) measurements. The CsPbI₂Br/J71 film has been prepared by spin-coating hot J71 solution (150 °C) onto the CsPbI₂Br surface, followed by thermal annealing at 150 °C for 10 min to induce secondary crystallization. From

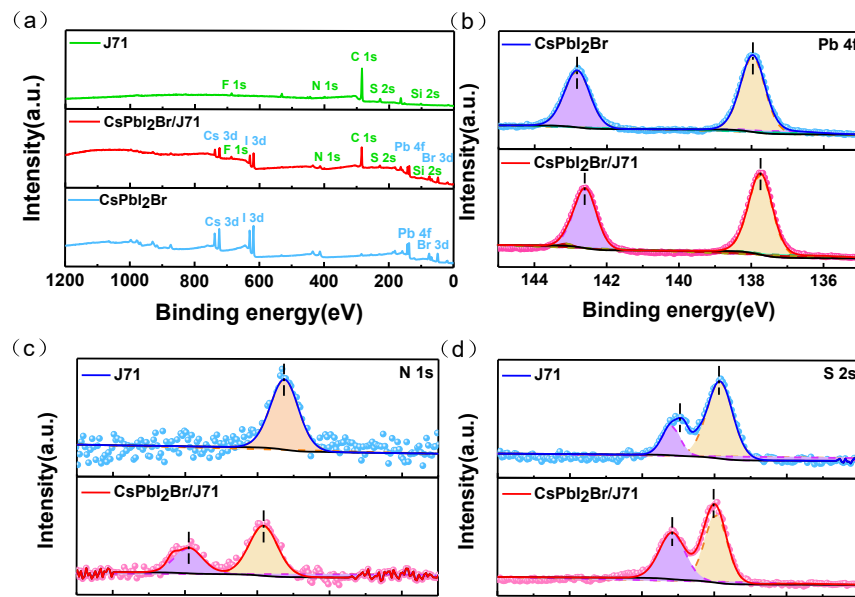
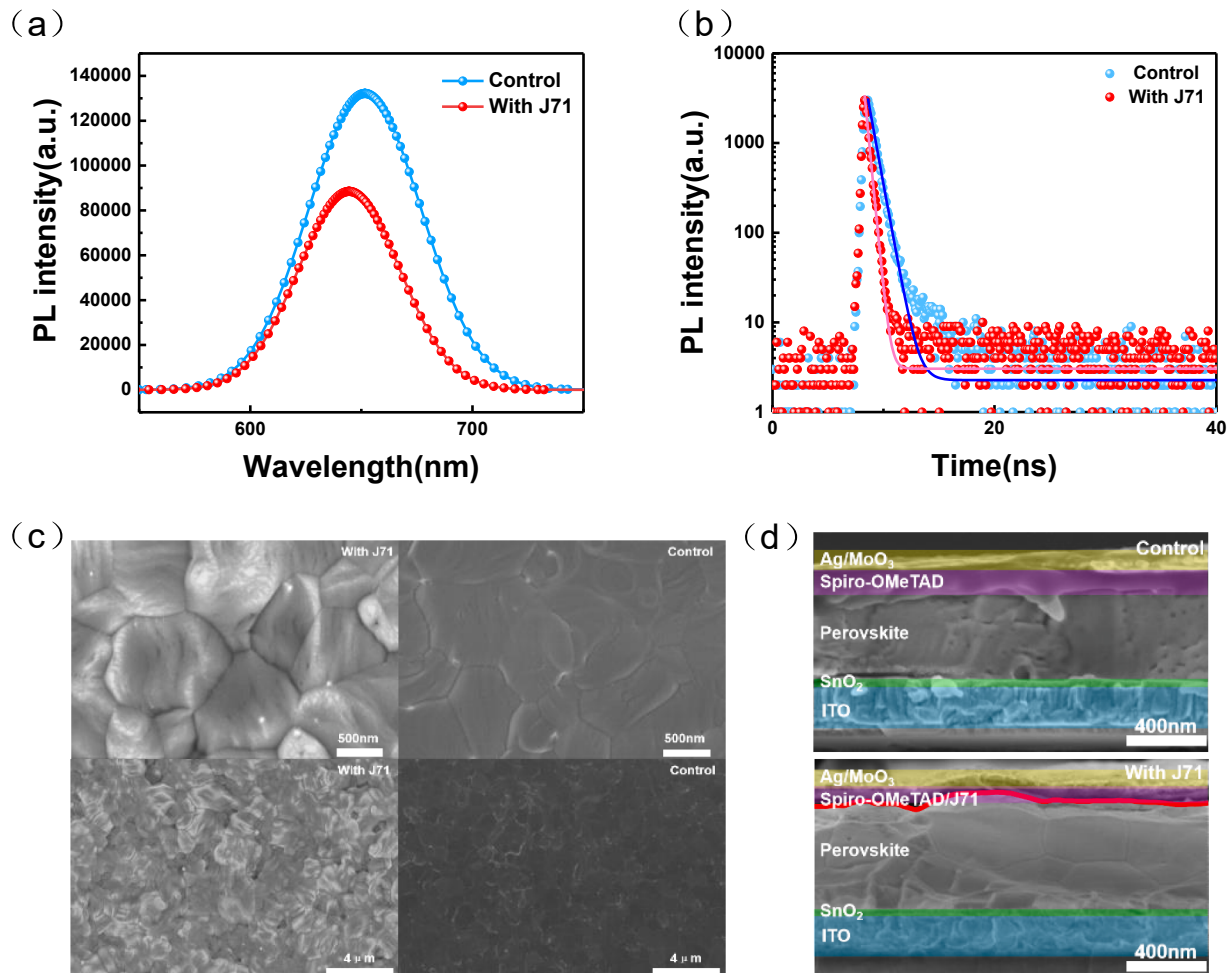


Fig. 2. (a) XPS survey spectra, (b) Pb 4f XPS, (c) N 1 s XPS, (d) S 2 s XPS.

Fig. 3. (a) Steady-state PL spectra and (b) TRPL spectra of control and $\text{CsPbI}_2\text{Br}/\text{J71}$ films, (c) SEM images: control and $\text{CsPbI}_2\text{Br}/\text{J71}$ films of different scales, (d) Cross-section SEM images: control and $\text{CsPbI}_2\text{Br}/\text{J71}$ devices.

the SEM images shown in Fig. 3c, it can be observed that CsPbI₂Br/J71 exhibits larger and more compact perovskite grains, with grain size exceeding 1 μm, which is advantageous to the photovoltaic performance in terms of less charge recombination. The result indicates the secondary crystallization induced by J71 is an effective means to refine the morphology and crystal growth dynamics of CsPbI₂Br, which expects to release the residual stress in the film [30]. The cross-sectional SEM pictures of the device are shown in Fig. 3d, we compared the growth of perovskite films between the control device and the modified device. It is found that the perovskite grains modified by J71 are denser and highly ordered. In addition, the pores of the whole film are significantly reduced. This is due to the fact that J71 molecule under heat treatment promotes the secondary crystallization of perovskite, which is consistent with the results shown in the previous surface SEM images.

To further dig into the effects of J71 on the residual stress in CsPbI₂Br film, a mechanical model has been established, as illustrated in Fig. 4a. Due to the thermal expansion mismatch between the CsPbI₂Br perovskite and the ITO/SnO₂ substrate, high temperature thermal annealing process would generate large residual stress in the CsPbI₂Br film. It thus leads to further expansion of lattice and increment of the spacing between crystal planes [31]. With J71 modification, N and S elements in J71 molecule bond with Pb in perovskite and produce force interactions, which could effectively offset the tensile stress in the crystal and shorten the crystal plane spacing. To quantitatively analyze the stress in CsPbI₂Br, the micro-structural morphology of both CsPbI₂Br and CsPbI₂Br/J71 are then scrutinized by high-resolution transmission electron microscope (TEM) measurement [32,33]. The lattices are analyzed by fast Fourier transform (FFT) [31]. From the results shown in Fig. 4b, the (211) plane spacing of perovskite are extracted to be 4.96 Å and 4.24 Å for the pristine CsPbI₂Br and CsPbI₂Br/J71 films, respectively. The reduced lattice spacing with J71 treatment agrees well with the model in Fig. 4b, which testifies the suppressed tensile stress in the CsPbI₂Br/J71 films.

The expansion or contraction of the CsPbI₂Br perovskite lattices under different strain conditions (at a variety of J71 concentrations) are subsequently analyzed by the Raman spectroscopy of Pb-I bond [5]. Theoretically, the strain-free α-CsPbI₂Br cubic phase has low Raman activity, with weak Pb-I Raman signals. As the in-plane tensile strain increases, the inorganic skeleton gradually obtains tetragonality and produces stronger Raman signal [34]. In Fig. 4c, the pristine CsPbI₂Br shows two peaks originating from the Pb-I bond. The main peak at 129 cm⁻¹ is caused by the stretching of in-plane Pb-I bond and the shoulder peak at 145 cm⁻¹ is due to the compression of out-plane Pb-I bond. From the spectrum, stretching is determined to be the main effect due to its higher intensity. With the increase of J71 concentration from 0.5 to 2 mg/mL, the Raman intensity decreases, indicating suppressed strain in the film [34]. To gain a deeper insight into how the tensile/compressive strain variates during J71 treatment, the Raman spectra are further normalized and fitted by Gaussian function [35]. As shown in Fig. 4d, with increasing the J71 concentration from 0.5 to 1 mg/mL, the main peak corresponding to the tensile strain experiences a gradual shift from 130.8 to 131.3 cm⁻¹, while the shoulder peak assigned to the compressive strain gradually shift from 144.9 to 143.7 cm⁻¹. It certifies that both tensile and compressive strains are weakened with J71 modification. When the concentration further incrementing to 2 mg/mL, the in-plane compression at 144.2 cm⁻¹ becomes dominated, indicating the strain condition has been reversed in the film. The result highly conforms to the mechanical model proposed in Fig. 4a, where the coordination between J71 and perovskite offers a compressive force to offset the tensile strain in the film, and the optimal concentration is found to be 1 mg/mL. In order to more accurately show the adjustment of J71 to internal stress, we carried out the characterization test of GIXRD for the optimal concentration and control films. The basic idea is fixing 20° and changing the tilting angle of the instrument while maintaining a constant X-ray penetration depth. We believe that perovskite films are quasi isotropic, so all the following discussions are based on the quasi

isotropic plane stress state. By adding 2θ Fit as sin2ψ As a function, we can calculate the perovskite film stress, and the slope of the fitting line represents the residual strain. The (012) plane at 31.7° is selected for analysis because it has a higher differential value and can provide more reliable structural information. As shown in Fig. 4e-f, by setting the inclination angle ψ Changing from 10° to 50°, the characteristic peak gradually experiences a blue-shift at different levels, indicating that the lattice constant expands along the in-plane direction. In general, the sin2ψ-2θ relationship is linear, and the negative slope of the fitting line indicates the existence of tensile stress in the perovskite film (Fig. 4g). Compared with the control film, the modified film shows a smaller slope (absolute value), indicating that the tensile strain is reduced, which agree well with our FTIR results.

Photovoltaic performances of PSCs based on the structure of ITO/SnO₂/CsPbI₂Br or with J71/Spiro-OMeTAD/MoO₃/Ag have then been studied, the devices are tested under simulated 1 sun illumination with intensity of 100 mW cm⁻². Fig. 5a evaluates the effects of J71 concentration on the device performances, and the photovoltaic parameters are summarized in Table 1. It is seen that increasing the J71 concentration to 1 mg/mL monotonously raising the PCE from 13.35% to 16.15%, with simultaneously improved open-circuit voltage (V_{OC}), short-circuit current density (J_{SC}) and fill factor (FF). This can be ascribe to the synergistic effects of J71 on forming cascade energy level alignment for better hole extraction, releasing the tensile strain of CsPbI₂Br for more effective charge conducting and refined crystallization for less charge recombination [36]. While further increasing the J71 concentration to 2 mg/mL drops the PCE to 15.20%. According to the previously discussion, this could be attributed to the compressive stress of CsPbI₂Br film caused by excess J71 incorporation. The results are in line with the Raman analysis. In addition, we studied the hysteresis of the device. The forward and backward sweep J-V curves and photovoltaic characteristics of the devices are shown in Fig. S1 and Table S2 respectively. The results show that the J71 modification suppressed the hysteresis of the device, which could be ascribed to the improved film quality and better charge transporting characteristics in the device. The external quantum efficiency (EQE) measurements have been conducted to evaluate J_{SC} of the device. From Fig. 5b, integration of the EQE spectra gives integrated J_{SC} of 14.77 and 15.24 mA cm⁻² for pristine CsPbI₂Br and CsPbI₂Br/J71 based PSCs, respectively, which are within 5% error as compared to those from the J-V characteristics. In order to verify the reliability of the device and the accuracy of photocurrent measurement, the stable power output of the device is monitored at the maximum power tracking point (MPP) for 200 s under full sunlight irradiation. As shown by Fig. 5c, the steady-state photocurrent of the device increases significantly in the first few seconds and eventually reaches stable J_{SC} of 14.72 and 15.49 mA cm⁻², which correspond to steady-state PCE of 12.95% and 15.95%, respectively. As shown in Fig. 5d and S2, we can clearly find that the device modified by J71 shows great reproducibility through the statistics of PCE of 30 devices, which once again proves that the treatment could be a promising means for the development of highly efficient and stable PSCs in the future [29,37].

In addition to the photovoltaic efficiency, we also studied the long-term stability of devices under N₂ and humidity environment, the results are shown in Fig. 5e-f. Compared with the control devices, the J71 modified ones show notably improved stability under both N₂ and RH 25% humidity environments, by retaining 85% of the initial PCE for 826 h in N₂, and 83% of the original PCE for 650 h in humid environment. In clear contrast, the control device already shows significant degradation during the first 100 h under both aging conditions. The improved stability under N₂ can be explained by the released tensile stress of the intrinsic CsPbI₂Br crystals upon J71 treatment. In terms of moisture stability, we note that J71 modification improves the hydrophobicity of the film surface by increasing the contact angle of perovskite film from 51.67° and 99.41° (as shown as Fig. S3) [38]. It thus provides a protection barrier for moisture evasion into the internal film, and circumvents the adverse effect of water molecules on triggering the lattice

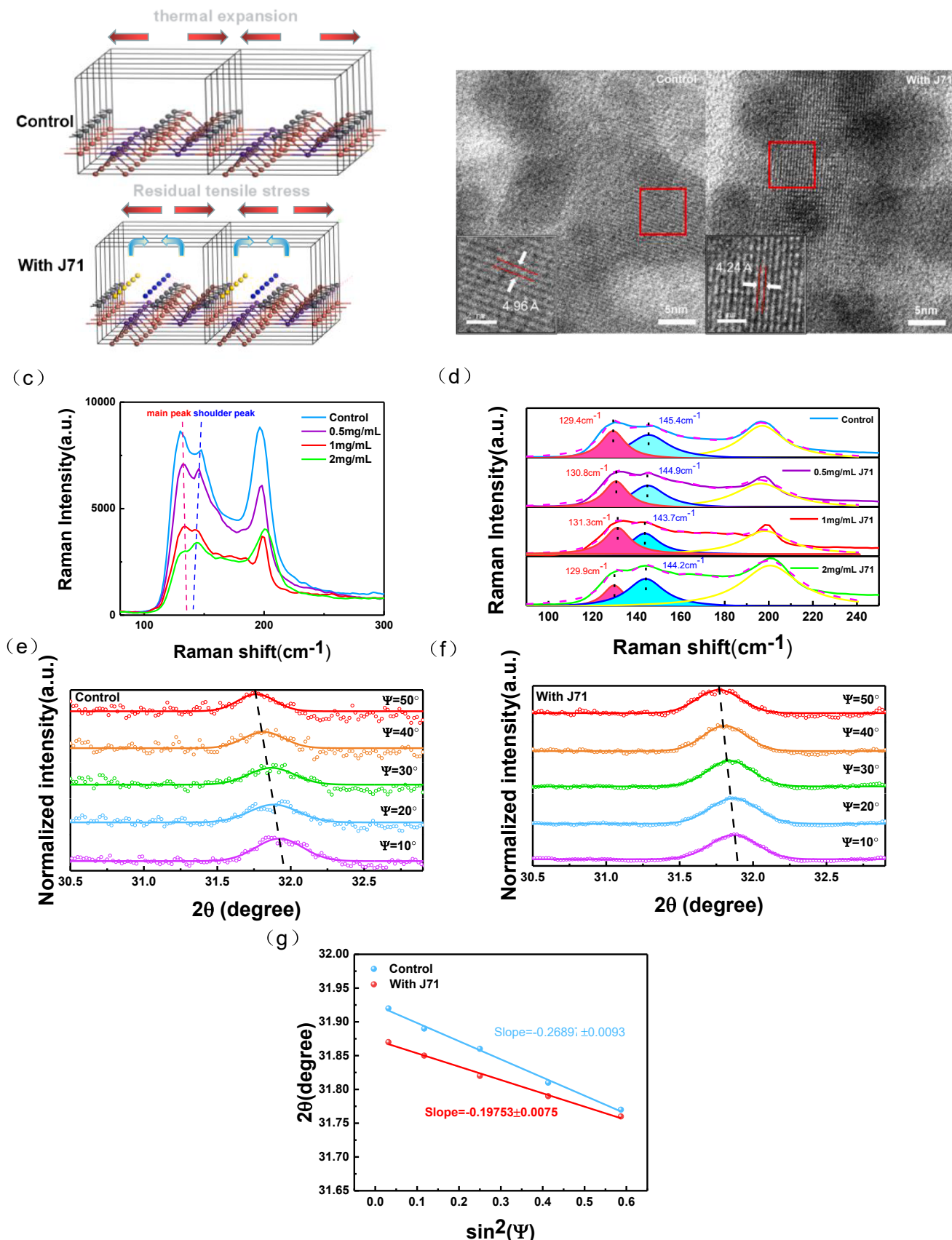


Fig. 4. (a) Crystal mechanics model of control and $\text{CsPbI}_2\text{Br}/\text{J71}$, (b) TEM images of control films and $\text{CsPbI}_2\text{Br}/\text{J71}$ films, (c) Confocal Raman spectra of the Pb-I bond with different J71 concentrations, (d) Fitting Raman peaks of the Pb-I bond with different J71 concentrations, (e) GIXRD spectra at different tilt angles of control, (f) GIXRD spectra at different tilt angles of perovskite with J71, (g) linear fit of $2\theta - \sin^2(\Psi)$ for perovskite films.

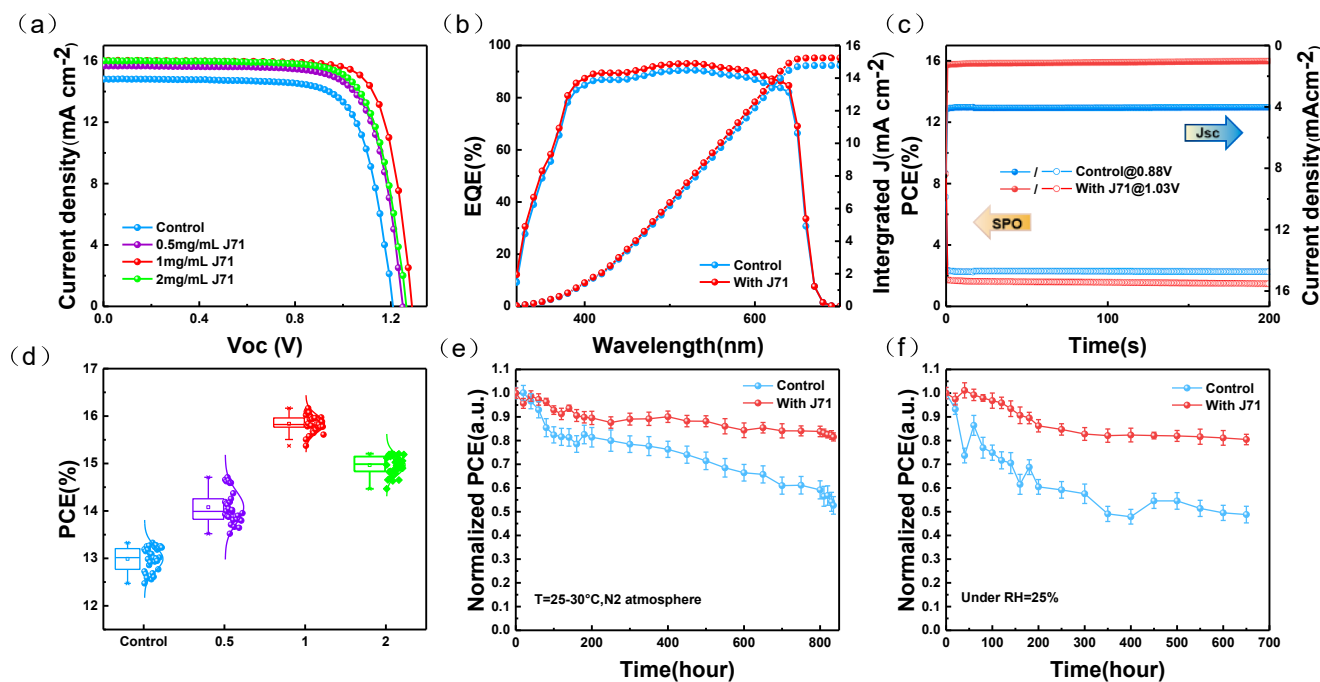


Fig. 5. (a) $J - V$ curves and (b) EQE spectra of the champion devices based on control and $\text{CsPbI}_2\text{Br}/\text{J71}$ films, (c) Steady-state current density and stabilized power output (SPO) at maximum-power point tracking under working conditions with 100 mW cm^{-2} irradiation, (d) PCE normal distribution of the devices based on control and $\text{CsPbI}_2\text{Br}/\text{J71}$ films, (e,f) Long-term stability test under N_2 and RH25% at room temperature.

distortion CsPbI_2Br . Phase stability of CsPbI_2Br have also been tested under high humidity environment (RH 70–80%). From Fig. S4, it is seen that the pristine CsPbI_2Br has been rapidly degraded within just 3 min, while $\text{CsPbI}_2\text{Br}/\text{J71}$ film can be stable for 30 min [39].

To analyze the charge recombination in the devices, the dependence of V_{OC} and J_{SC} on various light intensities (P_{light}) of PSCs are evaluated. The correlation between J_{SC} and light intensity (P_{light}) is shown in Fig. 6a. According to the formula: $J_{SC} \propto P_{light}^\alpha$ [40], the slope values α of the control and J71 modified devices are extracted to be 0.883 and 0.984, respectively. The α value close to 1 elucidates lower amount of monomolecular recombination in the PSC device, which conforms to our expectation. Similarly, the relationship between V_{OC} and P_{light} is presented in Fig. 6b, the light intensity dependence of V_{OC} shows a strong logarithmic relation, which can be described as the following formula: $V_{OC} \propto \left(\frac{n k T}{q}\right) \ln(P_{light})$ [41]. For pristine PSCs and J71 modified PSCs, the values of $n k T/q$, which represents the slop of logarithmic linear function, are determined to be 1.56 and 1.44 kT/q , respectively. The lower slope value closer to $1kT/q$ in the J71 treated PSCs suggests the dominated bimolecular charge recombination in the device, which implies decreased trap-assisted recombination [42].

In order to further prove the effect of J71 on the passivation of perovskite surface and the conductivity of interface hole, the hole mobilities of pristine CsPbI_2Br and $\text{CsPbI}_2\text{Br}/\text{J71}$ device are showed by the space-charge-limited current (SCLC) models. We fabricated the hole-only test device with the structure of ITO/PEDOT:PSS/ CsPbI_2Br /control or J71/Spiro-OMeTAD/MoO₃/Au. As shown in Fig. 6c, the $J - V$ characteristics can be divided into ohmic region under low bias voltage, trap filled limit region and trap free child region. We firstly analyze the ohmic region and trap-filled limited (TFL) region to estimate the density of trap states (n_{trap}) of both control and $\text{CsPbI}_2\text{Br}/\text{J71}$ films based on the equation $n_{trap} = \frac{2\xi_0\xi_e V_{TFL}}{el^2}$, where ξ is the relative dielectric constant of CsPbI_2Br (8.5), ξ_0 is the vacuum permittivity, e is the electron charge, and L is the thickness of the perovskite (about 430 nm). From Fig. 6c, the V_{TFL} of control and J71 modified devices are determined to be 0.41 V and 0.29 V, respectively, and the corresponding trap density of states are

calculated to be 2.09×10^{15} and $1.48 \times 10^{15} \text{ cm}^{-3}$, respectively. The results show that the Lewis complex formed by the coordination of J71 and Pb effectively inhibits the Pb hanging bond on the perovskite surface, and the trap state is greatly passivated. Then we analyze the child region of the SCLC models to compare the effect of J71 on hole transporting ability of PSCs. Based on the equation: $J = \frac{9}{8}\varepsilon_0\varepsilon_r\mu_h\frac{(V_a - V_{bi})^2}{L^3}$, where ε_0 is the permittivity of vacuum, ε_r is the relative dielectric constant, μ_h is the hole mobility, L is the thickness of perovskite film, V_a is the applied voltage and V_{bi} is the built-in field. The calculation results of the hole model are summarized in Table S3. It can be seen that μ_h of control and $\text{CsPbI}_2\text{Br}/\text{J71}$ films are 7.37×10^{-2} and $9.98 \times 10^{-2} \text{ cm}^2 \text{ V}^{-1} \text{ s}^{-1}$, respectively. The improved hole mobility could be accredited to the better energy level alignment and refined crystal morphology in terms of larger and more compact grains. Fig. 6e shows the $C^{-2}-V$ plots of two devices. It is seen that $\text{CsPbI}_2\text{Br}/\text{J71}$ exhibits larger V_{bi} of 0.83 V as compared to that of the control film (0.74 V). The larger V_{bi} will increase the driving force of photocarrier dissociation, which is conducive to the formation of extended depletion region and could effectively inhibit recombination. According to the Mott-Schottky equation: $C^{-2} = \frac{2(V_{bi} - V)}{N_d\varepsilon_0 A^2}$, where C is the capacitance under voltage bias, A is the area of devices, N_d is the charge density, and ε and ε_0 present the relative permittivity and vacuum permittivity, respectively [43], charge density (N_d) of the two devices are 2.213×10^{16} and $1.906 \times 10^{16} \text{ cm}^{-3}$, respectively. The decreased N_d at perovskite/J71 interfaces manifest reduced charge accumulation, which should be attributed to the improved charge extraction efficiency at the interface [44,45]. Fig. 6e shows the Nyquist plots. The composite resistance (Rrec) of the original device and the target device are 1379.0Ω and 3233.8Ω , respectively. Obviously, compared with the control device, the improved device shows greater composite resistance (Rrec), which indicates suppressed charge recombination in the J71 modified device. Therefore, the promoted V_{OC} and excellent FF can be attributed to the reduction of recombination in the device.

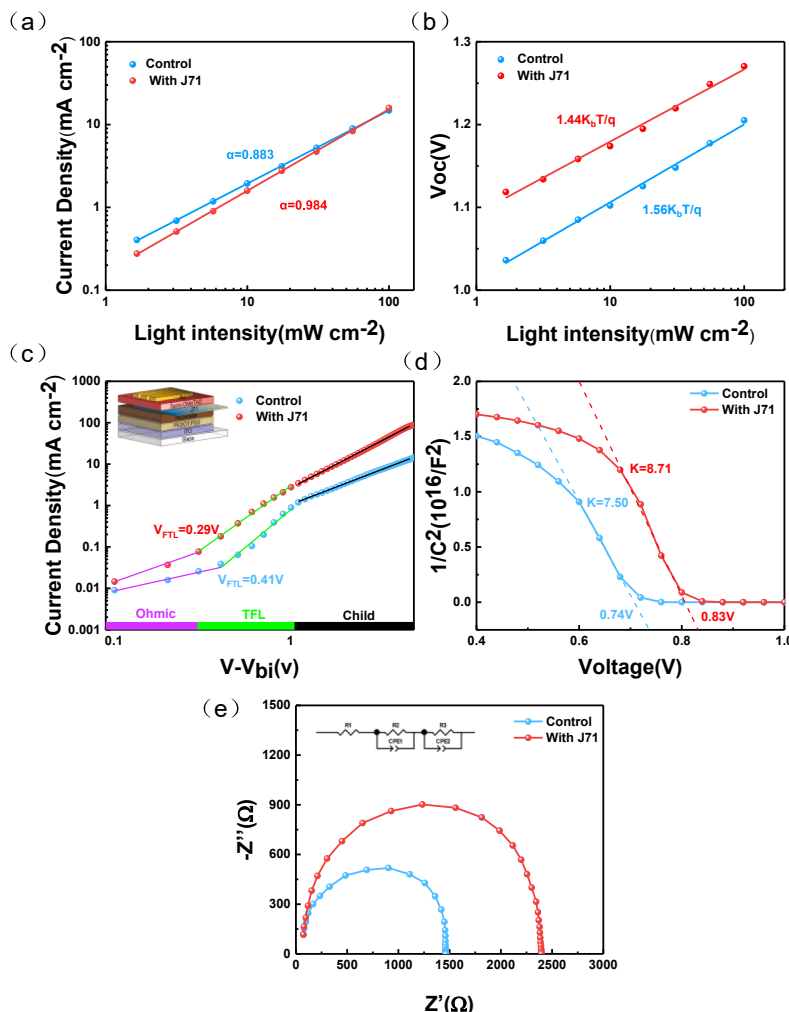


Fig. 6. (a) V_{OC} vs light intensity and (b) J_{SC} vs light intensity of solar cells based on control and CsPbI₂Br/J71 films, (c) $J - V$ characteristics of the hole-only devices based on control and CsPbI₂Br/J71 films, (d) Mott-Schottky spectra of solar cells based on control and CsPbI₂Br/J71 films, (e) Nyquist plots of Control and CsPbI₂Br/J71 PSCs.

4. Conclusion

In conclusion, the organic polymer J71 has been utilized in this work to release the residual stress in the CsPbI₂Br film. We found that the coordinating bond between J71 and perovskite could facilely modulate the strain-type from tensile to compressive, and the strain-free film could be obtained at an optimal J71 concentration. Additionally, the secondary crystal growth triggered by covalent bond between J71 and perovskite leads to refined CsPbI₂Br crystals, including larger perovskite grains and more compact crystal ordering, which could hamper charge recombination in the film. More importantly, the highly hydrophobic J71 serves as a moisture blocking layer, which could prevent the lattice distortion of $[\text{PbI}_6]^{4-}$ triggered by water molecules. As a result, over 16% PCE has been achieved by the PSCs with J71 treatment. The device shows excellent stability by retaining over 80% of the initial PCEs under both N₂ and humid environment.

Declaration of Competing Interest

The authors declare that they have no known competing financial interests or personal relationships that could have appeared to influence the work reported in this paper.

Acknowledgements

This work is financially supported by the National Key R&D Program of China (2017YFE0106000), National Science Fund for Distinguished Young Scholars (21925506), National Natural Science Foundation of China (22005322, 51773212, 81903743, 51875384), Ningbo S&T Innovation 2025 Major Special Programme (2018B10055), CAS Key Project of Frontier Science Research (QYZDB-SSW-SYS030).

Appendix A. Supplementary data

Supplementary data to this article can be found online at <https://doi.org/10.1016/j.cej.2022.137307>.

References

- [1] W. Xiang, S. Liu, W. Tress, A review on the stability of inorganic metal halide perovskites: challenges and opportunities for stable solar cells, *Energy Environ. Sci.* 14 (2021) 2090–2113.
- [2] N. Ouedraogo, N.A.N. Ouedraogo, Y. Chen, Y.Y. Xiao, Q. Meng, C.B. Han, H. Yan, Y. Zhang, Stability of all-inorganic perovskite solar cells, *Nano Energy* 67 (2020) 104249.
- [3] F.-Z. Qiu, M.-H. Li, S. Wang, Y. Jiang, J.-J. Qi, J.-S. Hu, Strain relaxation and domain enlargement via phase transition towards efficient CsPbI₂Br solar cells, *J. Mater. Chem. A* 10 (7) (2022) 3513–3521.

- [4] F. Ke, C. Wang, C. Jia, N.R. Wolf, J. Yan, S. Niu, T.P. Devereaux, H.I. Karunadasa, W.L. Mao, Y. Lin, Preserving a robust CsPbI₃ perovskite phase via pressure-directed octahedral tilt, *Nat. Commun.* 12 (2021) 461.
- [5] D.J. Xue, Y. Hou, S.C. Liu, M. Wei, B. Chen, Z. Huang, Z. Li, B. Sun, A.H. Proppe, Y. Dong, M.I. Saidaminov, S.O. Kelley, J.S. Hu, E.H. Sargent, Regulating strain in perovskite thin films through charge-transport layers, *Nat. Commun.* 11 (2020) 1514.
- [6] W. Chen, X. Li, Y. Li, Y.A. Li, review: crystal growth for high-performance all-inorganic perovskite solar cells, *Energy & Environ. Sci.* 13 (2020) 1971–1996.
- [7] Y. Chen, T. Shi, P. Liu, W. Xie, K. Chen, X. Xu, L. Shui, C. Shang, Z. Chen, H.L. Yip, G. Zhou, X. Wang, The distinctive phase stability and defect physics in CsPbI₂Br perovskite, *J. Mater. Chem. A* 7 (2019) 20201–20207.
- [8] C. Liu, W. Li, C. Zhang, Y. Ma, J. Fan, Y. Mai, All-Inorganic CsPbI₂Br Perovskite Solar Cells with High Efficiency Exceeding 13, *J. Am. Chem. Soc.* 140 (2018) 3825–3828.
- [9] W. Hui, Y. Xu, F. Xia, H. Lu, B. Li, L. Chao, T. Niu, B. Du, H. Du, X. Ran, Y. Yang, Y. Xia, X. Gao, Y. Chen, W. Huang, In situ observation of δ phase suppression by lattice strain in all-inorganic perovskite solar cells, *Nano Energy.* 73 (2020) 104803.
- [10] J. Duan, Y. Zhao, B. He, Q. Tang, High-Purity Inorganic Perovskite Films for Solar Cells with 9.72 % Efficiency, *Angew. Chem. Int. Ed.* 57 (2018) 3787–3791.
- [11] T. Ozturk, E. Akman, A.E. Shalan, S. Akin, Composition engineering of operationally stable CsPbI₂Br perovskite solar cells with a record efficiency over 17%, *Nano Energy.* 87 (2021) 106157.
- [12] S.S. Mali, J.V. Patil, P.S. Shinde, G.D. Miguel, C.K. Hong, Fully Air-Processed Dynamic Hot-Air-Assisted M:CsPbI₂Br (M: Eu²⁺, In³⁺) for Stable Inorganic Perovskite Solar Cells, *Matter.* 4 (2021) 635–653.
- [13] H. Guo, Y. Pei, J. Zhang, C. Cai, K. Zhou, Y. Zhu, Doping with SnBr 2 in CsPbBr₃ to enhance the efficiency of all-inorganic perovskite solar cells, *J. Mater. Chem. C.* 7 (2019) 11234–11243.
- [14] J. Duan, Y. Zhao, Y. Wang, X. Yang, Q. Tang, Hole-Boosted Cu(Cr, M)O₂ Nanocrystals for All-Inorganic CsPbBr₃ Perovskite Solar Cells, *Angew. Chem. Int. Ed.* 58 (2019) 16147–16151.
- [15] S.S. Mali, J.V. Patil, C.K. Hong, Making air-stable all-inorganic perovskite solar cells through dynamic hot-air, *Nano Today.* 33 (2020) 100880.
- [16] W. Xiang, Z. Wang, D.J. Kubicki, W. Tress, J. Luo, D. Prochowicz, S. Akin, L. Emsley, J. Zhou, G. Dietler, M. Grätzel, A. Hagfeldt, Europium-doped CsPbI₂Br for stable and highly efficient inorganic perovskite solar cells, *Joule.* 3 (2019) 205–214.
- [17] M.B. Faheem, B. Khan, C. Feng, M.U. Farooq, F. Raziq, Y. Xiao, Y. Li, All-inorganic perovskite solar cells: energetics, key challenges, and strategies toward commercialization, *ACS Energy Lett.* 5 (2019) 290–320.
- [18] J. Xue, R. Wang, K.L. Wang, Z.K. Wang, I. Yavuz, Y. Wang, Y. Yang, X. Gao, T. Huang, S. Nuryeyeva, J.W. Lee, Y. Duan, L.S. Liao, R. Kaner, Y. Yang, Crystalline liquid-like behavior: surface-induced secondary grain growth of photovoltaic perovskite thin film, *J. Am. Chem. Soc.* 141 (2019) 13948–13953.
- [19] H. Bin, L. Gao, Z.-G. Zhang, Y. Yang, Y. Zhang, C. Zhang, S. Chen, L. Xue, C. Yang, M. Xiao, Y. Li, 11.4% Efficiency non-fullerene polymer solar cells with trialkylsilyl substituted 2D-conjugated polymer as donor, *Nat. Commun.* 7 (1) (2016).
- [20] S. Wafee, B.H. Liu, C. Leu, Lewis bases: promising additives for enhanced performance of perovskite solar cells, *Mater.today.energy.* 22 (2021) 100847.
- [21] Y. Zhang, C. Wu, D. Wang, Z. Zhang, X. Qi, N. Zhu, G. Liu, X. Li, H. Hu, Z. Chen, L. Xiao, B.o. Qu, High Efficiency (16.37%) of Cesium Bromide—Passivated All-Inorganic CsPbI₂Br Perovskite Solar Cells, *Sol. RRL* 3 (11) (2019) 1900254.
- [22] Y. Zhao, Y. Wang, J. Duan, X. Yang, Q. Tang, Divalent hard Lewis acid doped CsPbBr₃ films for 9.63%-efficiency and ultra-stable all-inorganic perovskite solar cells, *J. Mater. Chem. A* 7 (12) (2019) 6877–6882.
- [23] K. Zheng, J. Ge, C. Liu, Q. Lou, X. Chen, Y. Meng, X. Yin, S. Bu, C. Liu, Z. Ge, Improved phase stability of CsPbI₂Br perovskite by released microstrain toward highly efficient and stable solar cells, *InfoMat.* 3 (2021) 1431–1444.
- [24] F. Li, C. Chen, F. Tan, C. Li, G. Yue, L. Shen, W. Zhang, Semitransparent inverted polymer solar cells employing a sol-gel-derived TiO₂ electron-selective layer on FTO and MoO₃/Ag/MoO₃ transparent electrode, *Nanoscale Res. Lett.* 9 (1) (2014).
- [25] T. Kong, H. Xie, Y. Zhang, J. Song, Y. Li, E.L. Lim, A. Hagfeldt, D. Bi, Perovskitoid-Templated Formation of a 1D@3D Perovskite Structure toward Highly Efficient and Stable Perovskite Solar Cells, *Adv. Energy Mater.* 11 (34) (2021) 2101018.
- [26] D. Ma, W. Li, X. Chen, Z. Yang, J. Zhao, Z. Yang, Y.i. Zhang, Z. Chi, An Effective strategy of combining surface passivation and secondary grain growth for highly efficient and stable perovskite solar cells, *Small* 17 (25) (2021) 2100678.
- [27] Q. Lou, G. Lou, R. Peng, Z. Liu, W. Wang, M. Ji, C. Chen, X. Zhang, C. Liu, Z. Ge, Synergistic effect of lewis base polymers and graphene in enhancing the efficiency of perovskite solar cells, *ACS Appl. Energy Mater.* 4 (2021) 3928–3936.
- [28] S. Fu, L. Wan, W. Zhang, X. Li, W. Song, J. Fang, Tailoring In Situ Healing and Stabilizing Post-Treatment Agent for High-Performance Inverted CsPbI₃ Perovskite Solar Cells with Efficiency of 16.67%. *ACS Energy Lett.* 5 (2020) 3314–3321.
- [29] S. Fu, W. Zhang, X. Li, J. Guan, W. Song, J. Fang, Humidity-assisted chlorination with solid protection strategy for efficient air-fabricated inverted CsPbI₃ perovskite solar cells, *ACS Energy Lett.* 6 (2021) 3661–3668.
- [30] Q. Luo, H.e. Ma, F. Hao, Q. Hou, J. Ren, L. Wu, Z. Yao, Y.u. Zhou, N. Wang, K. Jiang, H. Lin, Z. Guo, Carbon nanotube based inverted flexible perovskite solar cells with all-inorganic charge contacts, *Adv. Func. Mater.* 27 (42) (2017) 1703068.
- [31] X. Li, W. Chen, S. Wang, G. Xu, S. Liu, Y. Li, Y. Li, One-source strategy boosting dopant-free hole transporting layers for highly efficient and stable CsPbI₂Br perovskite solar cells, *Adv. Funct. Mater.* 31 (21) (2021) 2010696.
- [32] X. Liu, X. Wang, T. Zhang, Y. Miao, Z. Qin, Y. Chen, Y. Zhao, organic tetrabutylammonium cation intercalation to heal inorganic CsPbI₃ perovskite, *Angew. Chem. Int. Ed.* 60 (2021) 12351–12355.
- [33] Q. Lou, Y. Han, C. Liu, K. Zheng, J. Zhang, X. Chen, Q. Du, C. Chen, Z. Ge, π-conjugated small molecules modified SnO 2 layer for perovskite solar cells with over 23% efficiency, *Adv. Energy Mater.* 11 (39) (2021) 2101416.
- [34] Y. Chen, Y. Lei, Y. Li, Y. Yu, J. Cai, M.H. Chiu, R. Rao, Y. Gu, C. Wang, W. Choi, H. Hu, C. Wang, Y. Li, J. Song, J. Zhang, B. Qi, M. Lin, Z. Zhang, A.E. Islam, B. Maruyama, S. Dayeh, L.J. Li, K. Yang, Y.H. Lo, S. Xu, Strain engineering and epitaxial stabilization of halide perovskites, *Nature.* 577 (7789) 209–215.
- [35] X. Su, H. Ma, H. Wang, X. Li, X.X. Han, B. Zhao, Surface-enhanced Raman scattering on organic-inorganic hybrid perovskites, *Chem Commun.* 54 (2018) 2134–2137.
- [36] K. Wang, Z. Jin, L. Liang, H. Bian, D. Bai, H. Wang, J. Zhang, Q. Wang, S. Liu, All-inorganic cesium lead iodide perovskite solar cells with stabilized efficiency beyond 15%, *Nat Commun.* 9 (2018) 4544.
- [37] S. Fu, X. Li, L.i. Wan, Y. Wu, W. Zhang, Y. Wang, Q. Bao, J. Fang, Efficient Passivation with Lead Pyridine-2-Carboxylic for High-Performance and Stable Perovskite Solar Cells, *Adv. Energy Mater.* 9 (35) (2019) 1901852.
- [38] Y. Yang, Q. Yuan, H. Li, Y. Niu, D. Han, Q. Yang, Y. Yang, S. Yi, D.-Y. Zhou, L. Feng, Dopant free mixture of Spiro-OMeTAD and PTAA with tunable wettability as hole transport layer enhancing performance of inverted CsPbI₂Br perovskite solar cells, *Org. Electro.* 86 (2020) 105873.
- [39] X. Wang, Y. Wang, Y. Chen, X. Liu, Y. Zhao, Efficient and stable CsPbI₃ inorganic perovskite photovoltaics enabled by crystal secondary growth, *Adv. Mater.* 33 (44) (2021) 2103688.
- [40] Y. Liu, X. Zhao, Z. Yang, Q. Li, W. Wei, B. Hu, W. Chen, Cu₁₂Sb₄S₁₃ quantum dots with ligand exchange as hole transport materials in all-inorganic perovskite cspbi3 quantum dot solar cells, *ACS Appl. Energy Mater.* 3 (2020) 3521–3529.
- [41] Y.X. Luo, J. Chen, H.Y. Hou, Y.C. Ye, K.C. Shen, L. Lu, Y. Li, F. Song, X. Gao, J. X. Tang, Hierarchically manipulated charge recombination for mitigating energy loss in CsPbI₂Br Solar Cells, *ACS Appl. Mater. Interfaces* 12 (2020) 41596–41604.
- [42] T. Liu, J. Zhang, M. Qin, X. Wu, F. Li, X. Lu, Z. Zhu, A.-Y. Jen, Modifying surface termination of CsPbI₃ grain boundaries by 2D perovskite layer for efficient and stable photovoltaics, *Adv. Funct. Mater.* 31 (15) (2021) 2009515.
- [43] L. Ma, W. Zhang, P. Zhao, J. Liang, Y.i. Hu, G. Zhu, R. Chen, Z. Tie, J. Liu, Z. Jin, Highly efficient overall water splitting driven by all-inorganic perovskite solar cells and promoted by bifunctional bimetallic phosphide nanowire arrays, *J. Mater. Chem. A.* 6 (41) (2018) 20076–20082.
- [44] Q. Lou, H. Li, Q. Huang, Z. Shen, F. Li, Q. Du, M. Jin, C. Chen, Multifunctional CNT: TiO₂ additives in spiro-OMeTAD layer for highly efficient and stable perovskite solar cells, *EcoMat.* 3 (2021).
- [45] Y. Wang, C. Duan, X. Zhang, N. Rujisamphan, Y. Liu, Y. Li, J. Yuan, W. Ma, Dual Interfacial engineering enables efficient and reproducible CsPbI₂Br all-inorganic perovskite solar cells, *ACS Appl. Mater. Interfaces* 12 (2020) 31659–31666.